Prepared for submission to JINST

A Demonstration of Slowed Electron $\mathbf{E} \times \mathbf{B}$ Drift for PTOLEMY

M. Farino,[†1] **A. Tan,**[1] **and the PTOLEMY Collaboration: A. Apponi,**[2,3] **M. Betti,**[4,5] **M. Borghesi,**[6,7] **A. Casale,**[8] **O. Castellano,**[4,5] **G. Cavoto,**[4,5] **L. Cecchini,**[4] **E. Celasco,**[9] **W. Chung,**[1] **A.G. Cocco,**[10] **A. Colijn,**[11,12] **B. Corcione,**[4,5] **D. Cortis,**[10] **N. D'Ambrosio,**[10] **N. de Groot,**[13] **S. el Morabit,**[12] **A. Esposito,**[4,5] **M. Faverzani,**[6,7] **A.D. Ferella,**[10,14] **E. Ferri,**[6] **L. Ficcadenti,**[4,5] **S. Gamba,**[6,7] **S. Gariazzo,**[15] **H. Garrone,**[16,17,18] **F. Gatti,**[9] **A. Giachero,**[6,7] **Y. Iwasaki,**[19] **A. Kievsky,**[20] **M. Laubenstein,**[10] **F. Malnati**[17,18,21] **G. Mangano,**[21,22] **L.E. Marcucci,**[20,24] **C. Mariani,**[4,5] **J. Mead,**[12] **G. Menichetti,**[24,25] **M. Messina,**[10] **E. Monticone,**[17,18] **M. Naafs,**[11] **A. Nucciotti,**[6,7] **L. Origo,**[6,7] **F. Pandolfi,**[4] **D. Paoloni,**[2,3] **C. Pepe,**[17,26] **C. Pérez de los Heros,**[27] **O. Pisanti,**[23,24] **F.M. Pofi,**[10,28] **A.D. Polosa,**[4,5] **I. Rago,**[4] **M. Rajteri,**[17,18] **N. Rossi,**[10] **A. Ruocco,**[2,3] **S. Tayyab,**[4,5] **V. Tozzini,**[20,29] **C. Tully,**[1] **I. van Rens,**[13] **F. Virzi,**[10,14] **G. Visser,**[11] **M. Viviani,**[20] **U. Zeitler,**[13] **O. Zheliuk,**[13] **F. Zimmer**[12]

[1] *Princeton University, Jadwin Hall, Washington Rd, Princeton NJ, USA*

[2] *Istituto Nazionale di Fisica Nucleare (INFN), Sezione di Roma Tre, Via della Vasca Navale, 84, Roma, Italy*

[3] *Dipartimento di Scienze, Università degli Studi di Roma Tre, Via della Vasca Navale, 84, Roma, Italy*

[4] *Istituto Nazionale di Fisica Nucleare (INFN), Sezione di Roma, Piazzale Aldo Moro 2, 00185 Roma, Italy*

[5] *Sapienza Università di Roma, Piazzale Aldo Moro 2, 00185 Roma, Italy*

[6] *Istituto Nazionale di Fisica Nucleare (INFN), Sezione di Milano, Bicocca, Milano, Italy*

[7] *Dipartimento di Fisica, Università di Milano, Bicocca, Milano, Italy*

[8] *Department of Physics, Columbia University, New York, 538 West 120th Street, NY 10027, USA*

[9] *Università di Genova e INFN Sezione di Genova, Via Dodecaneso, 33, Genova, Italy*

[10] *Istituto Nazionale di Fisica Nucleare (INFN) Laboratori Nazionali del Gran Sasso, Via G. Acitelli, 22, Assergi, L'Aquila, Italy*

[11] *Nationaal instituut voor subatomaire fysica (Nikhef), Amsterdam, The Netherlands*

[12] *University of Amsterdam, Science Park 105, Amsterdam, The Netherlands*

[13] *Radbound University, Houtlaan 4, Nijmegen, The Netherlands*

[14] *Università degli Studi dell'Aquila, Palazzo Camponeschi, piazza Santa Margherita 2, 67100 L'Aquila, Italy*

[15] *Instituto de Física Teórica UAM-CSIC, C/Nicolás Cabrera 13-15 Campus de Cantoblanco, 28049, Madrid, Spain*

[16] *Department of Electronics and Telecommunications, Politecnico di Torino, 10129 Torino, Italy*

[17] *Istituto Nazionale di Ricerca Metrologica (INRiM), Str. delle Cacce, 91, Torino, Italy*

[18] *Istituto Nazionale di Fisica Nucleare (INFN), Sezione di Torino, Via P. Giuria, 1, Torino, Italy*

[19] *University of California, Berkeley, Berkeley CA, USA*

[†] Corresponding author.

arXiv:2503.10025v1 [physics.ins-det] 13 Mar 2025

[20]*Istituto Nazionale di Fisica Nucleare (INFN), Sezione di Pisa, Largo Bruno Pontecorvo, 3/Edificio C, Pisa, Italy*
[21]*Department of Applied Science and Technology, Politecnico di Torino, 10129 Torino, Italy*
[22]*Istituto Nazionale di Fisica Nucleare (INFN), Sezione di Naopoli, Compleso universitario di Monte S. Angelo ed. 6, via Cintia, Napoli, Italy*
[23]*Università degli Studi di Napoli Federico II, Corso Umberto I 40, Napoli, Italy*
[24]*Department of Physics, University of Pisa, Largo Bruno Pontecorvo, Pisa, Italy*
[25]*Istituto Italiano di Tecnologia, Graphene Labs, Via Morego 30, I-16163 Genova, Italy*
[26]*Institut de Microelectronica de Barcelona, IMB-CNM (CSIC), Bellaterra, 08193 Barcelona, Spain*
[27]*Uppsala University, 752 36 Uppsala, Sweden*
[28]*Gran Sasso Science Institute (GSSI), Viale Francesco Crispi, 7, L'Aquila, Italy*
[29]*Istituto Nanoscienze-CNR, Lab NEST-SNS, Pisa, Italy*

E-mail: mfarino@princeton.edu

Abstract: The novel transverse electromagnetic filtering system proposed by the PTOLEMY collaboration necessitates the precise control of β-decay electron motion via $\mathbf{E} \times \mathbf{B}$ drift. In particular, drift speed must be slowed substantially to contain electrons within the radio-frequency antenna region and accurately tune voltage potentials within the filter. This paper presents the experimental design to vary $\mathbf{E} \times \mathbf{B}$ drift speed of ^{14}C β-decay electrons using a custom electrode field cage situated between the pole faces of an electromagnet. Matching our results with high-fidelity simulation, we deduce a capacity to increase particle time of flight by a factor of 5 in the field cage's slow drift region. Limited only by the dimensions of our system, we assert drift speed can be arbitrarily slowed to meet the needs of PTOLEMY's future detector.

Keywords: Vacuum-based detectors, Detector modelling and simulations II (electric fields, charge transport, multiplication and induction, pulse formation, electron emission, etc), Trigger detectors, Instrumentation and methods for time-of-flight (TOF) spectroscopy

Contents

1 Introduction **1**
- 1.1 Neutrino Mass Experiments and Status 1
- 1.2 The PTOLEMY Experiment 2
- 1.3 **E × B** Transport 3

2 E × B Demonstrator Design **4**
- 2.1 Concept 4
- 2.2 Field Cage 4
- 2.3 β Emission Source 5
- 2.4 PIN Diode Detector 5
- 2.5 Electronics and Readout Chain 8
- 2.6 Layout and Magnet 9

3 Procedure **12**
- 3.1 Operational Settings 12
- 3.2 Waveform Analysis 12
- 3.3 Modes of Operation 14

4 Results **16**
- 4.1 Symmetric Slow Drift 16
- 4.2 Window Voltage Scans 16

5 Particle Simulations **17**
- 5.1 Particle Spectra 17
- 5.2 Comparison to Data 18
- 5.3 Time of Flight Estimation 20

6 Outlook **22**

A Beta Spectrometer **25**

1 Introduction

1.1 Neutrino Mass Experiments and Status

Juxtaposed to the Standard Model of particle physics, the discovery of neutrino oscillations [1, 2] necessitates a nonzero effective neutrino mass m_β, though it has yet to be precisely measured.[1] The

[1] $m_\beta = \sqrt{\sum_{i=1}^{3} |U_{ei}|^2 m_i^2}$, where m_i and U_{ei} denote neutrino mass eigenstates and electronic mixing matrix elements, respectively.

current model-independent upper limit on m_β is 0.45 eV/c^2 (90% confidence level), as set by the Karlsruhe Tritium Neutrino (KATRIN) experiment [3]. However, KATRIN and similar molecular tritium ($^3H_2$) experiments are limited to a sensitivity of $m_\beta \approx 0.2$ eV/c^2 due to broadening caused by internal molecular motion [4, 5] and background from surface radioimpurities [6]. Instead using *atomic* tritium (^{3}H), recently proposed projects such as PTOLEMY suggest that advances in our understanding of neutrino physics and techniques for high-sensitivity instrumentation could significantly improve sensitivity to measuring m_β [7, 8].

1.2 The PTOLEMY Experiment

PTOLEMY aims to create a scalable neutrino mass measurement experiment that performs precision spectroscopy of electrons produced near the endpoint energy from the β-decay of ^{3}H (equation 1.1). With strong background suppression and high energy resolution, distortions of the emission spectrum endpoint would enable a direct measurement of m_β. Tritium was selected for multiple reasons, including long lifetime and low Q-value ($\approx$ 18.6 keV) [9]. The proposed target substrate is graphene [10], which can efficiently store atomic tritium by binding it to carbon atoms. Extensive work is currently being undertaken by the collaboration and community at large to study the solid state effects on the β emission spectra [11–14].

$$^3\mathrm{H} \rightarrow {}^3\mathrm{He} + e^- + \bar{\nu}_e \tag{1.1}$$

To suppress background, PTOLEMY employs a technique called *cyclotron radiation emission spectroscopy* (CRES), which was pioneered by the Project 8 collaboration [15, 16]. Using radio-frequency (RF) antennas, an electron's kinetic energy is inferred by the relativistic frequency shift of the emitted cyclotron radiation. In the case of a near-endpoint electron, this information is used to guide the particle toward the calorimeter region. Provided enough time to obtain a large cyclotron radiation signal, CRES has been shown to be highly precise and stringently limit backgrounds near the tritium endpoint [17], enabling the possibility of direct differential energy measurement in time coincidence following a non-destructive CRES RF tag.

To attain high measurement resolution, PTOLEMY utilizes transition-edge sensor (TES) microcalorimeters, which precisely measure energy via the strongly temperature-dependent resistance of a cryogenic superconducting material's phase transition. In order for tritium endpoint electrons to fall within the dynamical range of the TES, static electromagnetic fields are used to reduce their kinetic energy from 18.6 keV to roughly 10 eV. This is performed by PTOLEMY's novel *transverse drift filter* [18]. The filter uniquely orients both the magnetic field gradient and electric field orthogonal to the magnetic field, resulting in components of the electron's motion driven by $\nabla\mathbf{B}$ and $\mathbf{E} \times \mathbf{B}$. This allows for a compact, scalable detector, with each dimension on the order of 1 meter [19]. In total, this technique could achieve an energy resolution as small as 50 meV [20], opening the possibility to a detection of the Cosmic Neutrino Background [9, 21] in addition to an effective neutrino mass measurement. A schematic of the PTOLEMY prototype is shown in Figure 1.

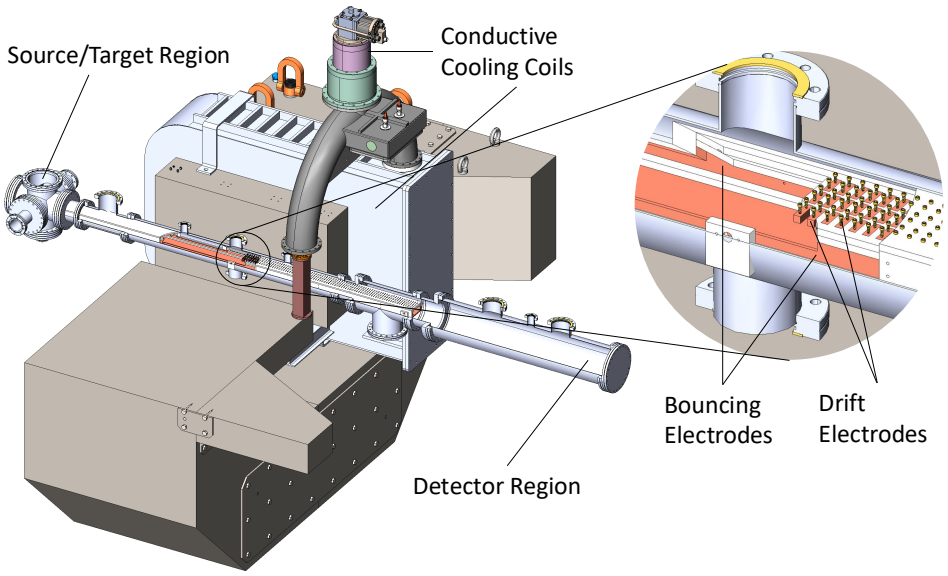

Figure 1: Schematic representation of the PTOLEMY prototype with conductive cooling MgB_2 coils. Electrons are emitted from the source/target region and enter the uniform **B**-field region, where a transverse electric field induces an $\mathbf{E}\times\mathbf{B}$ drift. Within the highlighted section, RF tracking occurs in the uniform **B**-field region between the pole faces, while transverse drift takes place in the decaying **B**-field region, guided by the fringe field shaping extensions, gradually reducing the electrons' energy. The bouncing electrodes provide additional control over electron trajectories in the longitudinal direction, ensuring efficient transport through the system. Finally, the electrons are directed toward the detector region, where their residual energy is precisely measured.

1.3 E × B Transport

$\mathbf{E}\times\mathbf{B}$ drift has been extensively researched in the contexts of plasma dynamics, propulsion, and astrophysical phenomena (for instance: [22], [23], and [24]), though is seldom employed deliberately for charged particle transport.[2] While there are studies involving the use of $\mathbf{E}\times\mathbf{B}$ drift to control low-energy positrons [25], contain secondary electrons [26], and create an angular-selective calibration source [27], PTOLEMY's concept of *slow* $\mathbf{E}\times\mathbf{B}$ drift for low-energy electron transport is entirely novel. Tethered to the strength of **E**, an electron's drift velocity can easily be changed by adjusting voltage potentials throughout the system. This feature is crucial to precisely reduce drift velocity near the RF antennas such that there is enough time (on the order of 100 μs [28]) to obtain a large enough signal to accurately tag electrons. This paper presents the design and characterization of a setup to demonstrate such slow drift of β-decay electrons.

[2]For a particle exposed to an electric field **E** while undergoing cyclotron motion due to a magnetic field **B** (satisfying $E^2 < c^2B^2$), the *drift velocity* of its guiding center (the center point of circular cyclotron motion) is given as $\mathbf{v}_E = \frac{\mathbf{E}\times\mathbf{B}}{B^2}$ and commonly referred to as $\mathbf{E}\times\mathbf{B}$ drift.

2 E × B Demonstrator Design

2.1 Concept

The conceptual setup for the demonstrator is shown in Figure 2. Eight electrode plates are situated between the pole faces of a magnet. Two of these electrodes, the *bouncing electrodes*, are oriented parallel to the magnet pole faces and supplied with a negative voltage to create a potential barrier to contain electrons within the apparatus (such that the electron motion parallel to the magnetic field exhibits a *bouncing* behavior), similar to the electrostatic mirror described in [29]. The remaining six are organized into three pairs of vertically offset *drift electrodes*, with voltages applied to generate an electric field orthogonal to the magnetic field. The potential difference between the center pair of plates is set to be smaller than that of the outer pairs, thereby creating a region of slower drift. In total, an electron injected through one end of the demonstrator undergoes cyclotron motion, bounces between bouncing electrodes, and drifts toward the other end. An example of such a trajectory is shown from a top-down orientation in Figure 3. The increased density of trajectory lines in the center region indicates slower drift. This Figure and all subsequent simulation estimates are generated using CST Studio Suite by Dassault Systèmes [30].

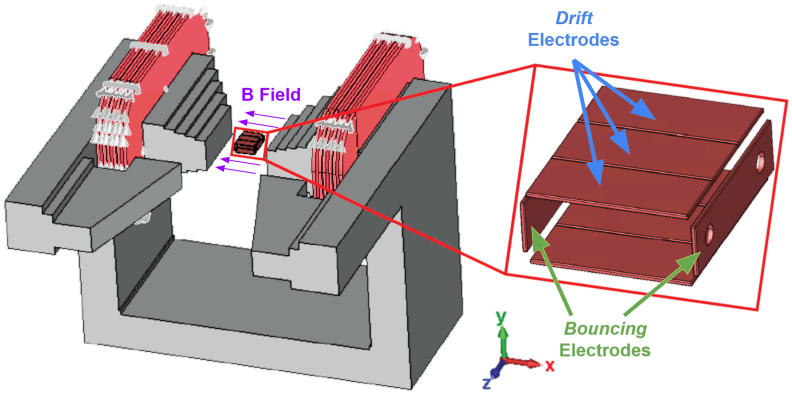

Figure 2: Conceptual demonstrator setup. Electrode plates are positioned between a magnet's pole faces, where a uniform magnetic field is generated (shown in purple). The plates (enlarged on the right) consist of two bouncing electrodes (green) and six drift electrodes (blue). The bouncing electrodes are oriented parallel to the magnet pole faces and supplied with a negative potential to contain electrons within the system. The six drift electrodes are organized into three vertically offset pairs that produce an electric field orthogonal to the magnetic field. The potential difference in the center drift plates is set to be smaller than the outer plates, facilitating slower $\mathbf{E} \times \mathbf{B}$ drift. Following the included axes, the magnetic field is negatively oriented along the x-direction and the electric field (produced by the drift electrodes) is oriented along the y-direction, resulting in $\mathbf{E} \times \mathbf{B}$ drift in the z-direction.

2.2 Field Cage

At the forefront of actualizing the design shown in Section 2.1 is a *field cage* to hold the electrodes. Assembled with machined Teflon parts and plastic screws, the custom-built cage fixes the relative positions of all eight copper electrode plates. Teflon was chosen for its excellent insulation properties and quick outgassing in vacuum. Two bouncing electrodes (96.8 mm × 25.4 mm × 2.4 mm) span

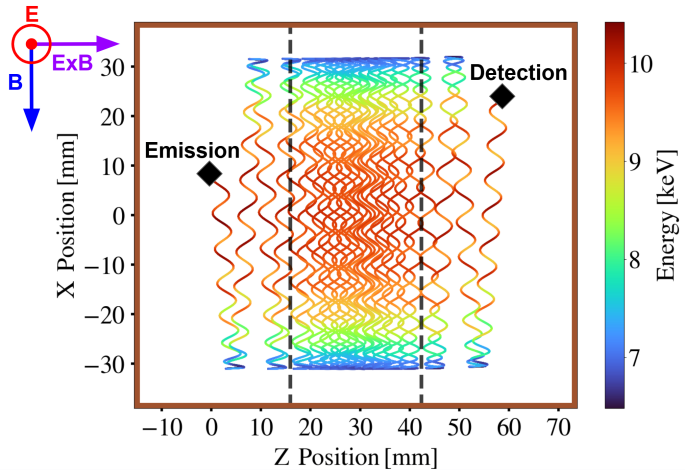

Figure 3: Top-down trajectory of a 10 keV electron within the demonstrator. The electron exhibits cyclotron motion while bouncing between two electrodes and drifting rightward due to potential differences in the other six. A smaller difference on the center pair of drift electrodes (marked by dashed vertical lines) results in slowed drift, as evidenced by an increased density of trajectory lines. Emission and detection points of the electron are denoted with black diamonds. The direction of the electric field (red), magnetic field (blue), and **E** × **B** drift (purple) are included in the upper left corner. The brown outline represents the outer perimeter of the electrode plates. In total, emitted electrons drift approximately 6 cm.

the length of the cage on both sides. Two holes (10.2 mm diameter) were bored into one of these electrodes originally for electron injection/detection, though are utilized to spatially fix additional components in the final setup. The outer (76.2 mm × 31.8 mm × 2.4 mm) and slightly thinner central (76.2 mm × 25.4 mm × 2.4 mm) drift plates are separated by plastic spacers of thickness 4 mm to prevent electrical sparking [31]. These plates lay flat on a tray and are fixed by a cover that screws into the bouncing electrode clamps. The upper and lower trio of plates are separated vertically by 31.8 mm. The design and an 'exploded' view of the casing including labeled parts are shown in Figure 4. The outward-facing Polyetheretherketone (PEEK) screws and cap hex nuts ensure the field cage remains fixed when situated inside a 10.2 cm outer diameter (OD) vacuum chamber as shown in Figure 5.

2.3 β Emission Source

^{14}C was selected as a suitable beta emitter for its relatively similar Q-value (155 keV) to tritium. The specific source used is a 10 μCi ^{14}C deposition with an aluminized Mylar window on a 25.4 mm diameter laminate disk manufactured by Spectrum Techniques. As ^{14}C is a sole beta emitter, an activity of 10 μCi corresponds to an emission rate of 370,000 electrons per second. The source disk (2π solid angle) emits half of that (i.e., 185,000 electrons per second), which was verified with a Geiger counter. The aluminized Mylar window allows the source to safely withstand vacuum-level pressures. A schematic is shown in Figure 6.

2.4 PIN Diode Detector

For electron identification, the system size and operating environment necessitate the use of a detector that is both compact and resilient to high magnetic fields. Inspired by the utilization of

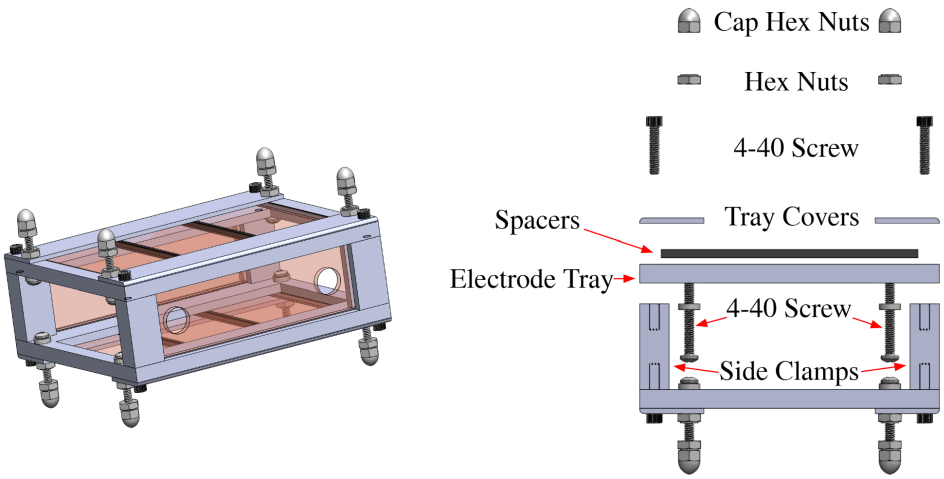

Figure 4: (a): Field cage design to fix the relative position of electrode plates. Components consist of machined Teflon pieces and commercially available plastic screws, washers, and hex nuts. (b): Exploded view of field cage with labeled parts. Bouncing electrodes are held via clamps, and the trios of drift electrodes lay on a tray fixed by a screwed-in cover. Drift electrodes are separated by 4 mm spacers to prevent electrical shorting, and the outward-facing screws and cap hex nuts are used to fix the field cage in a vacuum chamber.

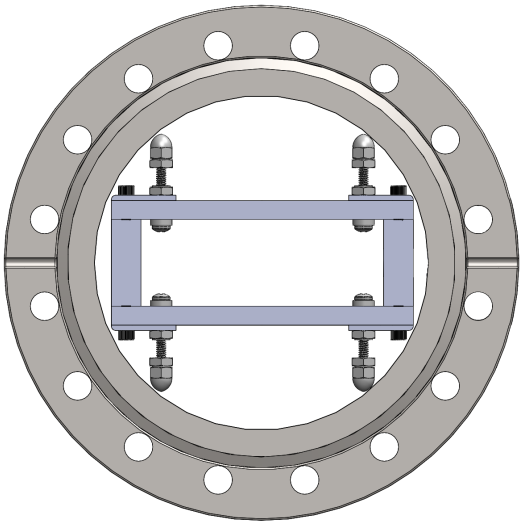

Figure 5: Side profile of the field cage situated in a 10.2 cm OD vacuum chamber. The cap hex nuts are adjusted to prevent movement of the field cage while in operation.

PIN diodes for low-energy electron detection by KATRIN [32], the OSRAM BPX 61 Silicon PIN diode was selected as a detector for this study. The specific model was chosen for its commercial availability and comparatively low cost. PIN diodes are electrical components containing an undoped intrinsic semiconductor region between a p-type and n-type semiconductor. When operated in reverse bias, they are sensitive to energy depositions of charged particles and light. The BPX

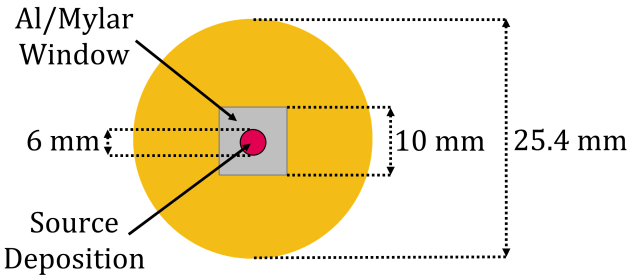

Figure 6: Schematic of ^{14}C disk used as β source in this study. The red dot indicates the 10 μCi deposition of the radioactive source, and the grey square represents the aluminized Mylar window. ^{14}C was selected for its relatively similar Q-value to tritium. The design of the source disk allows for it to safely withstand vacuum-level pressures.

61 additionally features a low dark current of 2 nA and a relatively large active detection area (7.02 mm^2), limiting electrical noise while increasing possible event count. However, commercial diodes — including the BPX 61 — are typically hermetically sealed by plastic or glass to prevent damage to the semiconductor region. Such covers, though providing little impedance to light, have a great enough stopping power to entirely prevent low-energy electron detection. For our study, the cover was carefully removed and the exterior casing was flattened to the base of the diode, improving sensitivity to higher-energy electrons with larger cyclotron radii. A heat shrink tube was attached around the neck of the diode to prevent torsion/bending from magnetization. An image of the BPX 61 diode and an example of the performed alterations are shown in Figures 7.

(a) (b)

Figure 7: BPX 61 diode (a) unaltered and (b) altered with removed glass cover, flattened casing, and heat shrink tube wrapping. This diode was selected as our detector for its commercial availability and low cost. Alterations to the device were performed to enable low-energy electron detection in a high magnetic field.

Energy threshold characterization of the device was performed using a beta spectrometer (details provided in Supplementary Material). In summary, the spectrometer sequentially selects energy range windows of transmittable electrons, and the PIN diode records counts of events during each iteration. Events are considered to be waveforms whose peak height exceeds a value of 45

mV above baseline after amplification (the electronic and amplification chain are identical to those discussed in Section 2.5). Based on the phase space of allowed particle trajectories in the system (discussed in Section 5), we situate the diode at a shallow angle ($\approx 20°$) with respect to the instrument aperture. In Figure 8, we present a relative trigger efficiency curve for the device obtained from beta spectrometer counts, observing a half-maximal trigger efficiency occurring at $\approx$ 70 keV. To clarify, this result does not reflect the true sensitivity of the device, but rather the trigger efficiency at a threshold safely above the noise floor of our subsequent data-taking conditions. Following manufacturer specifications, we assign an energy resolution of 11%.

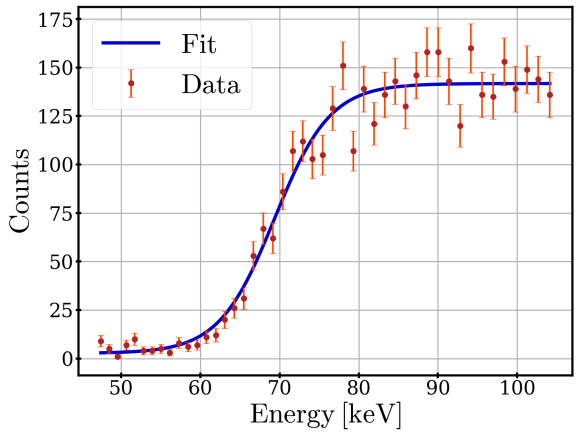

Figure 8: Diode energy threshold characterization using a beta spectrometer. Shown are counts of recorded events (with Poisson statistic error bars) as a function of emitted particle energy, as well as a relative trigger efficiency curve fit to the data. A half-maximal trigger efficiency is seen to occur at roughly 70 keV.

2.5 Electronics and Readout Chain

Electrode voltage potentials are supplied by the CAEN Model DT8034 8-channel power supply, featuring a long term (1 week) voltage stability of ±1.2 V, as well as maximum voltage and current settings of ±6 kV and 1 mA, respectively. Hence, the maximum potential barrier available to set on the bouncing electrodes is −6 kV, and the maximum potential difference between drift electrodes is 12 kV ($\Rightarrow |\mathbf{E}| = (12\,\text{kV})/(0.03175\,\text{m}) \approx 378\,\text{kV/m}$). Current flows via a safe high voltage (SHV) connector directly to brackets soldered onto the electrodes as shown in Figure 9.

A reverse bias voltage of 25 V is supplied to the BPX 61 diode by a Keithley 6487 picoammeter/voltage source. Operating at a reverse voltage slightly below the maximum setting (32 V) was done to prevent any undue damage to the modified detector. Pulses from the diode are read out using the commercially available Cremat CR-150-R6 Charge Sensitive Preamplifier (CSP) evaluation board. The board is configured following the company's recommendations for operating a device with dark current below 10 nA, and the CR-110-R2.2 CSP module was selected to attain the highest possible gain (1.4 V/pC) with low noise (equivalent noise charge of 200 electrons). Powering the board are two 9 V batteries so as to electrically isolate the device from any deviations/noise in wall power. Signals are then amplified at a second stage using an Ortec model 572 shaping amplifier with a gain of 25 and shaping time of 2 μs. Finally, the output is read by a PicoScope 6404 USB PC oscilloscope; signal pulses exceeding a certain cutoff threshold are automatically saved by the

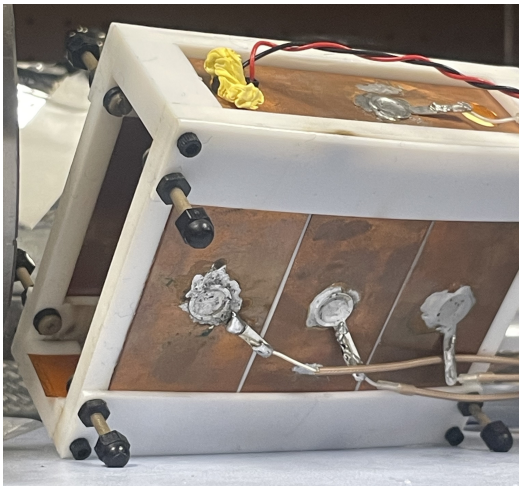

Figure 9: Wires supplying voltages are soldered directly to brackets on electrodes. The maximum voltage supplied is ±6 kV.

device for further analysis. A block diagram of the electronic readout chain and power supplies is shown in Figure 10. In this study, the PicoScope waveform voltage range is selected to be ±100 mV with an offset of −80 mV. We set a trigger at −50 mV, meaning any waveform with an amplified pulse at least 30 mV above baseline is stored.

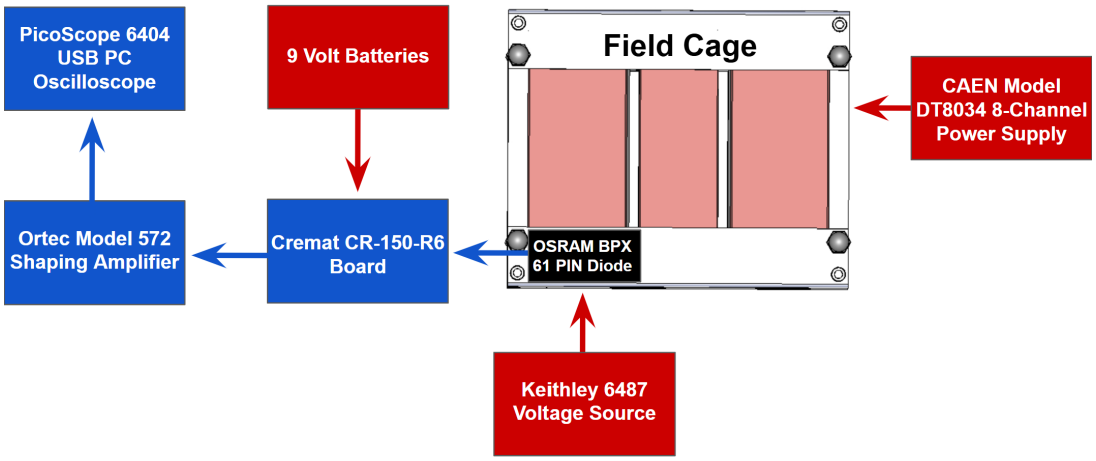

Figure 10: Block diagram showcasing various electrical components, including the detector (black), power supplies (red), and electronic readout chain (blue) for the setup.

2.6 Layout and Magnet

Using a Teflon block and tape, the ^{14}C source disk is fixed between one of the outer pairs of drift electrodes and centered between the bouncing electrodes. The disk is tilted at 60° with respect to the magnet pole faces. Considering drift velocity constraints imposed by the CAEN power supply, preliminary simulations indicated that nearly all emitted electrons terminated on the face of the source disk when oriented parallel to the magnet pole faces, meaning that electrons rarely drifted

far enough upon the first bounce to clear the entire source disk radius (12.7 mm). An example of a terminated trajectory for a 70 keV electron is shown in Figure 11. Tilting the disk was the simplest and safest method to reduce the necessary drift length and improve clearance likelihood. Thus, electrons emitted from the 60° tilted source only need to drift 6.35 mm to clear the disk. Repurposing the vestigial electron injection holes, the PIN diode detector is securely fixed between the other set of outer drift electrodes using Teflon tape. Inner electrode faces are additionally lined with Kapton polyimide film (76.2 μm thick) to mitigate electron scattering. Materials with a higher atomic number have a greater probability of scattering incident particles, making Kapton ($Z \approx 7$) a suitable cover for copper ($Z = 29$) to reduce scattering frequency. Top-down and side profiles of the field cage layout are shown in Figures 12.

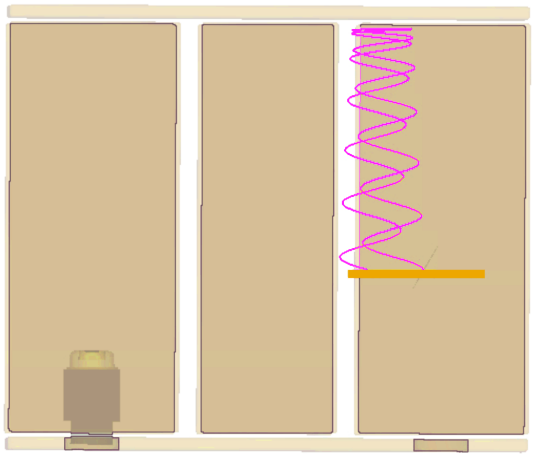

Figure 11: 70 keV electron trajectory (magenta) terminating on the face of the source disk (yellow) when oriented parallel to the magnet pole faces. This example illustrates the low likelihood an emitted electron drifts far enough to clear the source disk radius (12.7 mm), motivating our decision to rotate the source by 60°.

The field cage is placed within a 10.2 cm OD stainless steel vacuum chamber. The inner wall is lined with Kapton film (adhered by vacuum grease) to prevent electrical shorting between the chamber and electrode plates, as shown in Figure 13. The bulk of the chamber is placed adjacent to the magnet's pole faces (rotationally fixed by foam blocks), with connectors for vacuum pumping, voltage supply, and readout situated farther away from the high magnetic field region. Using a molecular drag pump, the system is held at a pressure of roughly 0.1 mPa. A picture of the full system layout is shown in Figure 14. The glass window flange allows for precise alignment of the field cage in relation to the magnet. When the system is operating, the flange is covered with blackout sheets.

The magnet consists of six coils (three on each side) powered by Walker Scientific Inc. HS-96-302 and HS-1575-4SS power supplies. Under maximum current conditions, a uniform magnetic field of $\approx$ 1 T is generated between the pole faces. For this study, we operate at a much lower setting to produce a field of $\approx$ 160 mT. Given that $\mathbf{v}_E = E/B$ for orthogonal fields, a lower magnetic field increases the maximal drift velocity and hence likelihood for electrons to clear aforementioned obstacles. Under these conditions, maximal drift velocity is given as $E/B \approx 2.4 \times 10^6$ m/s.

(a) (b)

Figure 12: (a): Top-down field cage layout with ^{14}C source disk (yellow) tilted at 60° and diode (silver and black) fixed via injection hole. (b): Side profile of field cage layout, showcasing the diode's Teflon fixture and Kapton film (to mitigate scattering) lining electrode plates.

Assuming the distance between the detector and source disk to be roughly 60 mm and ignoring effects due to the cyclotron radius, the estimated electron time of flight when operating all six drift electrodes at ±6 kV is $(0.06\ \text{m})/(2.4 \times 10^6\ \text{m/s}) = 25$ ns.

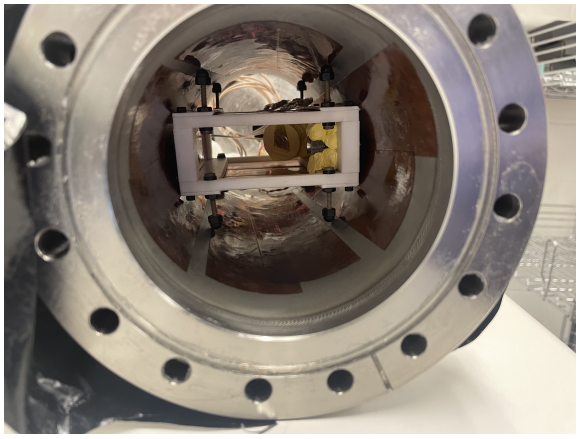

Figure 13: Field cage situated in 10.2 cm OD stainless steel vacuum chamber with inner walls lined by Kapton polyimide film to prevent electrical shorting between the chamber and electrode plates.

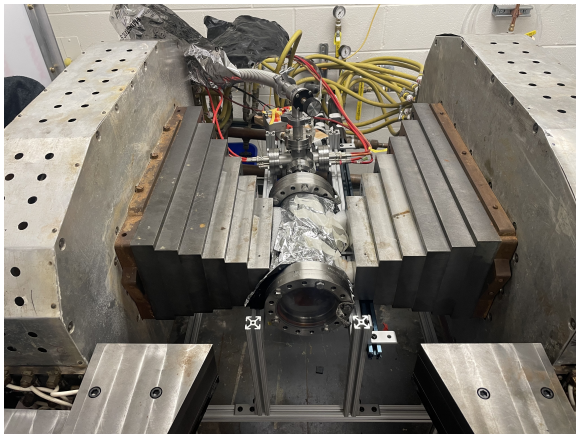

Figure 14: Field cage and vacuum chamber fixed between magnet pole faces with auxiliary components (connectors for voltage, electronic readout, and vacuum pumping) placed away from the high magnetic field region (top of image). The pressure is maintained at roughly 0.1 mPa, and the glass window flange is covered with blackout sheets when in operation. In this study, a uniform magnetic field of 160 mT is produced between the pole faces.

3 Procedure

3.1 Operational Settings

Following the orientation of the magnetic field (pointing leftward in Figure 14), an *upward* electric field is required to produce $\mathbf{E} \times \mathbf{B}$ drift directed toward the diode. This implies the lower and upper outer drift electrodes are respectively set to +6 and −6 kV for maximal drift velocity and source disk clearance. The center pair of drift electrodes is set at a smaller voltage difference to achieve slower drift (for instance +2 and −2 kV for 1/3 maximal drift velocity). Field orientation and an example voltage setting for the field cage are shown in Figure 15. Data is recorded operating the bouncing electrodes at *both* −6 and 0 kV. As electrons are capable of traveling through the system (and being detected by the PIN diode) by means of scattering off of the bouncing electrode plates, the difference in rates between these settings represents the event rate of successfully transported (i.e., bouncing) electrons. For any voltage setting, data-taking for the 0 kV bouncing electrode mode is performed between repeated runs of the −6 kV mode to ensure consistent behavior of the system.

3.2 Waveform Analysis

Waveform information stored by the PicoScope for triggered pulses is used to filter spurious events (including noise chirps or inverted pulses due to unstable electrical ground) from the data. We apply lenient ($\geq$ 98% efficient for most data runs) selection criteria to multiple regimes of the 200 μs time domain saved for each event (100 μs before and after the pulse trigger). These criteria applied to the mean (μ) and standard deviation (σ) of the waveform during various selected time domains are outlined in Table 1. Examples of waveforms that pass and do not pass such requirements are shown in Figures 16. For passing waveforms, the amplitude of the pulse height is proportional to the energy deposition of the impinging particle.

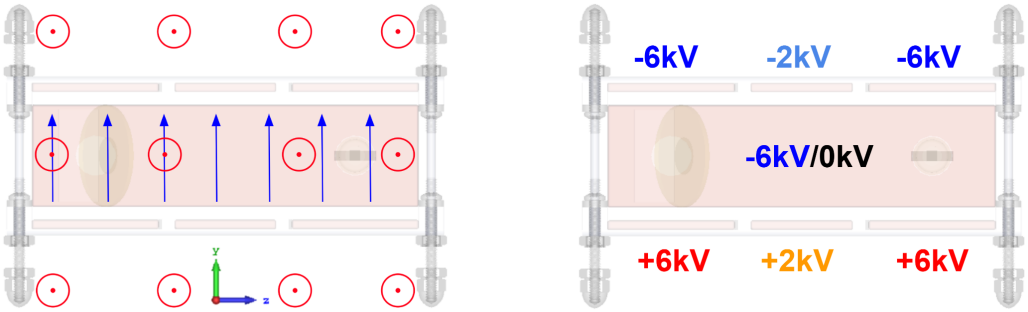

(a) (b)

Figure 15: (a): Orientation of **B** (red) and **E** (blue) to generate $\mathbf{E} \times \mathbf{B}$ drift towards detector. **E** is variably set by voltage differences between electrodes. (b): Voltage settings for electrode plates to obtain 1/3 maximal drift in the center region. Data is recorded operating the bouncing electrodes at both -6 and 0 kV; the difference between these settings represents the event rate of successfully transported electrons.

Table 1: Selection criteria on waveform mean (μ) and standard deviation (σ) over selected time periods of 200 μs saved output for each triggered event. In most data runs, $\geq 98\%$ of events pass these selection criteria.

Time Domain	**Selection Criterion**
$[90\ \mu s, 96\ \mu s]$	$\mu > -87$ mV
$[116\ \mu s, 124\ \mu s]$	$\mu \leq -77$ mV
$[140\ \mu s, 180\ \mu s]$	$2\text{ mV} < \sigma \leq 80$ mV

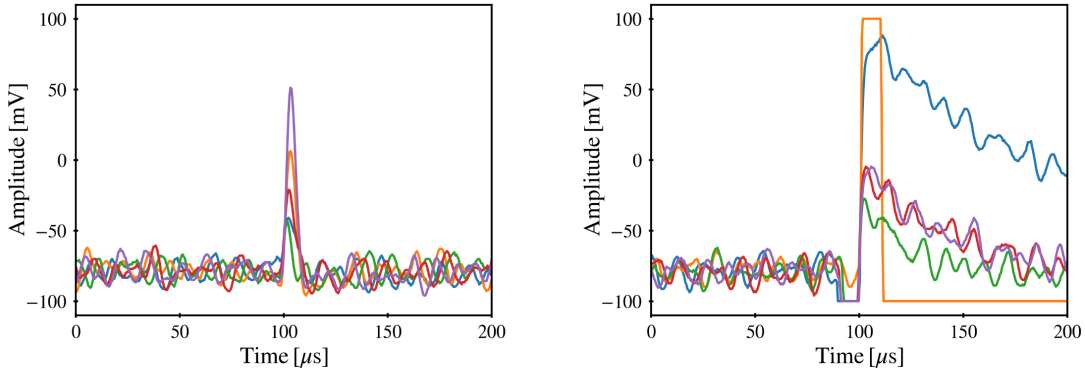

(a) (b)

Figure 16: Example waveforms (a) passing and (b) not passing the mean and standard deviation selection criteria outlined in Table 1. As mentioned previously, the baseline of waveform output is offset by -80 mV. The peak height above baseline of passing waveforms is proportional to the energy deposition of the impinging particle on the detector.

Once waveform analysis is performed, events are binned into a histogram according to their peak height (with the offset baseline shifted back to 0 mV). These bin counts are then divided by

the data acquisition time (normally on the order of 900 seconds) to obtain an event rate for various slow drift voltage settings. An example of such outputs including Poisson statistic error bars is shown in Figure 17 for the central drift electrode setting of ±2 kV. The significantly higher — and consistent — event rate with bouncing plates operated at −6 kV compared to 0 kV indicates successful transport of electrons. Statistical separation is most pronounced in the smaller voltage bins, while the spectra tend to converge at larger voltage bins — suggesting that the detection of higher-energy electrons is more heavily influenced by scattering. Events with pulse heights exceeding the range of the PicoScope are included in the highest voltage bin (known as an overflow bin).

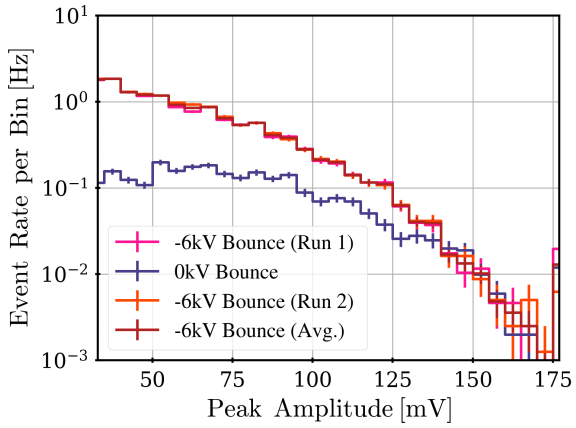

Figure 17: Binned event rates for ±2 kV central drift electrode setting for various bouncing electrode settings. Event rates are obtained by binning waveforms according to peak height and dividing each bin value by the data acquisition time (normally ≈ 900 seconds). The difference in event rate (particularly in smaller bins) between −6 kV and 0 kV bounce electrode settings indicates successful electron transport. Multiple −6 kV bounce runs are taken to ensure consistent system behavior. Uncertainties on each bin are assigned according to Poisson statistics.

3.3 Modes of Operation

Two methods are presented to probe characteristics of the $\mathbf{E}\times\mathbf{B}$ slow drift demonstrator: *symmetric slow drift* and *voltage scan* (both shown in Figure 18). Symmetric slow drift studies the change in event rate as the magnitude of the central drift plate voltages is *symmetrically* reduced (keeping a potential of 0 V at the midplane). Using CST, the top row of Figure 19 shows that potential lines disperse outward as the center potential difference decreases (displayed is a cross-section of the center plane in the demonstrator, though is representative of the field in general). With fewer potential lines remaining continuous, lower total event rates are expected for smaller central drift settings ($\mathbf{E}\times\mathbf{B}$ does no work, necessitating the guiding center of an emitted electron to follow potential lines of the orthogonal $\mathbf{E}$ field).

Alternatively, a voltage scan maintains a constant potential difference in the central plates (for instance a 2 kV 'window') but alters the midplane potential (central plate settings of +1 and −1 kV, +2 and 0 kV, +3 and +1 kV, etc.). As seen in the bottom row of Figure 19, only certain potential lines remain continuous depending on the midplane potential. The angled source disk — which more frequently emits particles pointed *towards* the diode than *away* — transmits electrons more

often with guiding centers in the upper half of the field cage. A maximal event rate is thus expected at a negative midplane voltage. Results are presented for both 1 kV and 2 kV window voltage scans.

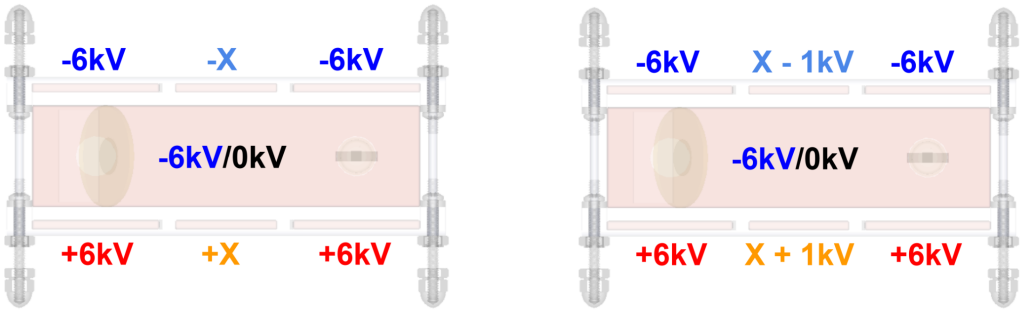

(a) (b)

Figure 18: (a): Symmetric slow drift setting, in which upper and lower central electrode plates are set to the same voltage **X** though opposite polarities, and are gradually decreased. (b): Window voltage scan setting, in which potential difference between upper and lower central electrode plates is maintained at a fixed value (e.g., 2 kV), though offset by various *midplane* voltage **X**. These are the two data-taking methods used to probe characteristics of the demonstrator.

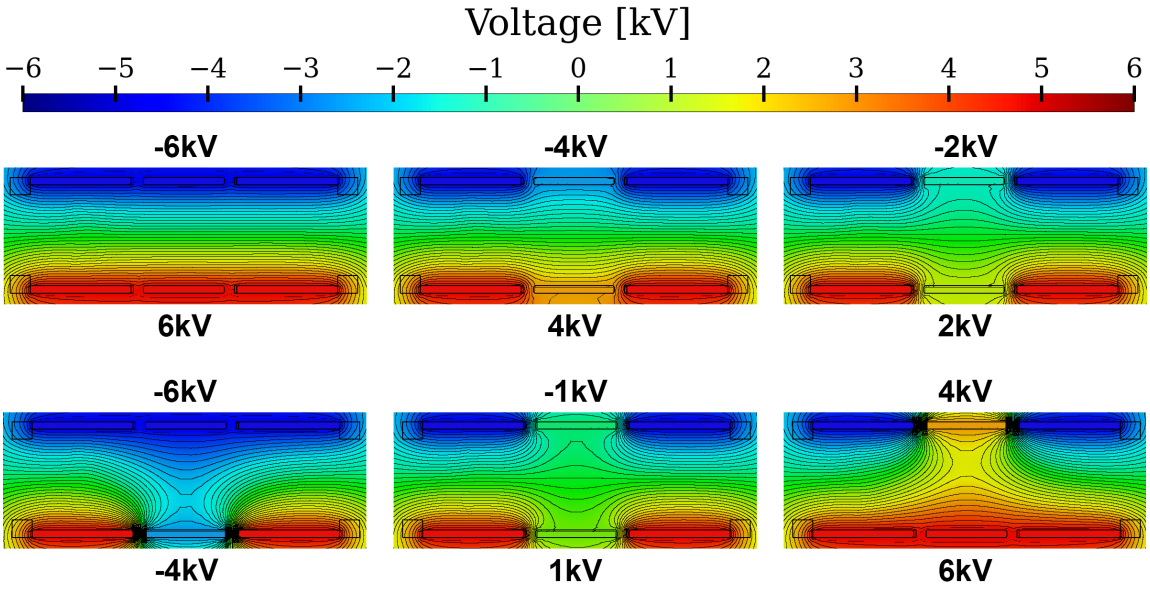

Figure 19: Potential lines for various symmetric slow drift (top row) and 2 kV window voltage scan (bottom row) settings. For symmetric slow drift, potential lines disperse outward as the center potential difference decreases, meaning lower event rates are expected for smaller potential differences. In the case of the voltage scans, only certain potential lines remain continuous; a maximal event rate is expected at a negative midplane voltage due to the angled source disk.

4 Results

4.1 Symmetric Slow Drift

Event rates, including error bars from Poisson statistics, of successfully transported electrons are shown in Figure 20 for various symmetric central drift electrode voltage settings. Settings are reported according to the voltage magnitude set to both central drift plates (i.e., 6 kV corresponds to lower and upper plates set at ±6 kV, etc.). Central electrode settings with a larger potential difference have a higher event rate for nearly every voltage bin and longer high voltage tail. To study the total event rate for each potential setting, we sum values in all bins above 45 mV (a threshold well above the noise level of the system and consistent with the PIN diode calibration using the beta spectrometer) in Figure 21. A fractional uncertainty of 16% (applied also to window voltage scans) was determined via repeated measurements under slightly altered conditions (noise level, magnetic field strength, chamber orientation, etc.). The distribution exhibits regimes of steep and plateauing event rate as a function of the center potential difference (and a maximal event rate of roughly 10 events per second at ±6 kV). Notably, potential differences approaching zero maintain a *nonzero* event rate, suggesting the residual field produced by the outer/bounce plates facilitates drift for small central plate settings.

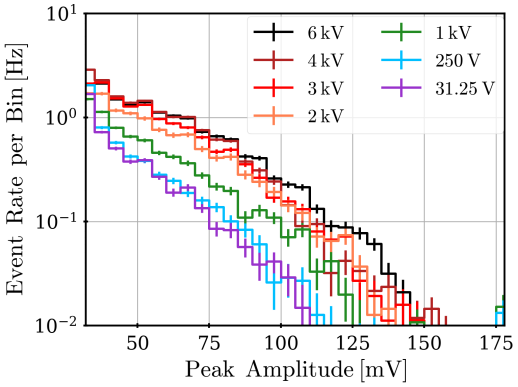

Figure 20: Binned event rates of successfully transported (i.e., difference in event rate of −6 kV and 0 kV bounce settings) electrons for various symmetric slow drift settings. Settings are reported as the potential magnitude set to both central drift plates. Those with a larger potential have a higher event rate for nearly every voltage bin and longer high voltage tail.

4.2 Window Voltage Scans

Similarly, cumulative event rates are tabulated and plotted as a function of the midplane voltage setting (i.e., average of top and bottom center plates) for both 2 kV and 1 kV window scans in Figure 22. Both distributions are roughly centered around −1 kV and event rates of the 1 kV scan are chiefly smaller than their 2 kV scan counterparts. In Section 5.2, we compare these results with CST counterparts to verify the accuracy of the simulated model.

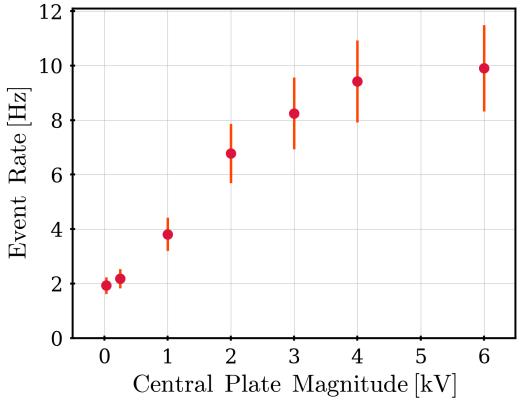

Figure 21: Cumulative event rates (above 45 mV) of successfully transported electrons for various symmetric slow drift settings. The distribution features regions of steep and plateauing event rate increase, a maximal event rate of 10 events per second at ±6 kV, and a nonzero event rate at ±0 kV. A fractional uncertainty of 16% is assigned to each event rate based on repeated measurements.

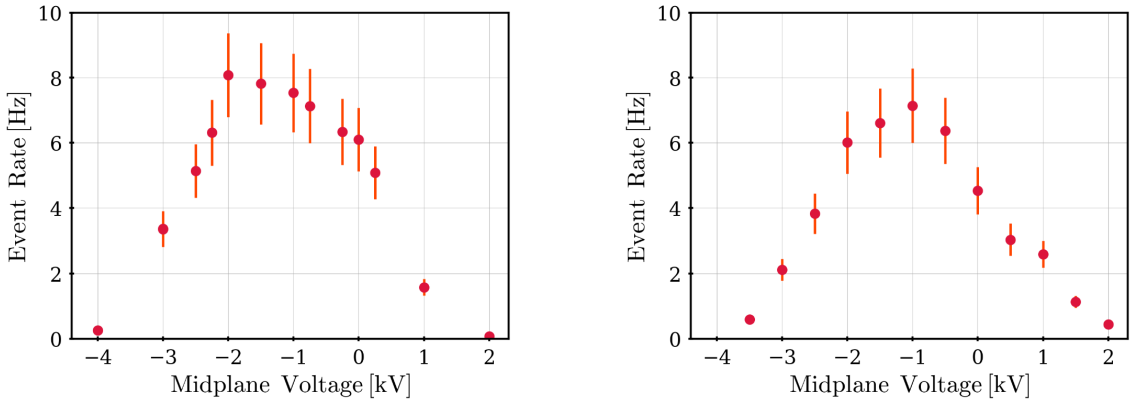

(a) (b)

Figure 22: Cumulative event rates (above 45 mV) of successfully transported electrons for various (a) 2 kV and (b) 1 kV window settings plotted as a function of midplane voltage. Both distributions are roughly centered around −1 kV, and the 1 kV window event rates are smaller than the 2 kV window counterpart for the same midplane voltage setting. Again, a fractional uncertainty of 16% is assigned to each event rate based on repeated measurements.

5 Particle Simulations

5.1 Particle Spectra

Importing design files into the software, the demonstrator was replicated in CST, and simulations were run under a multitude of voltage settings. To qualitatively understand the phase space of transmitted electrons, we record trajectories of emitted particles. This, for instance, allows us to confirm the proposed asymmetrical transmitted phase space of electrons as suggested in Section 3.3 (Figure 23). Trajectory information, however, is highly computationally intensive and places stringent limits on the number of electrons we can simulate. For more quantitative estimates, we

instead record the final location of each particle using the 2D particle monitor feature. This enables us to simulate 1 million electrons (2π solid angle and uniform energy ranging between 0 and 160 keV), corresponding to a few seconds of emission from the ^{14}C source. From the monitor, we save electrons whose terminal location corresponds to the active region of the diode ($\lesssim 0.04\%$ emitted). The output provides details on the phase space of electron transmission, including incident angle with the diode surface, which was the motivation for angling the diode for energy calibration as specified in Section 2.4. An example of such an output with the diode face overlaid is shown in Figure 24. The active area of the diode is situated 3.25 mm downward relative to the height of the ^{14}C emission source. As the relative height between the two in the physical setup is mildly ambiguous (i.e., the radioactive material on the source disk could have been deposited anywhere within a few mm from the disk center), this offset was chosen as its resultant spectrum most closely resembles data.

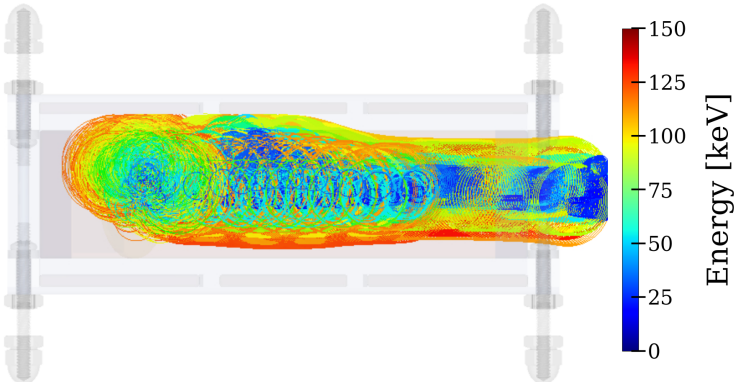

Figure 23: Asymmetry of emitted electron trajectories under symmetric +2 and −2 kV central voltage settings. This serves as a qualitative confirmation in simulation of our assessment that angling the source disk favors electrons with guiding centers in the upper half of the field cage. The computational intensity of trajectory information limits more quantitative assessments.

To obtain accurate event rates for comparison with data, counts are first binned by energy. These bin values are then divided by the total number of emitted electrons (1 million) and multiplied by the source activity (5 μCi). This, however, is the event rate as given from a *uniform* energy emission source. To obtain an event rate reflective of the source emission spectrum, each bin is finally weighted according to the normalized, discretized product of the ^{14}C β spectrum (smeared by the detector's 11% energy resolution) and the PIN diode trigger efficiency curve shown in Figure 25. The sum of these bins produces event rates which we compare directly to data.

5.2 Comparison to Data

Cumulative event rates obtained from CST are presented in Figure 26, exhibiting slightly higher values than their Section 4 counterparts. We demonstrate a correspondence between the two trios of distributions in Figure 27, fitting according to least squares for a scaling factor and horizontal offset (for the 1 kV and 2 kV windows). Event rates from CST are interpolated, and a $\pm 1\ \sigma$ confidence interval is tabulated accounting for Poisson statistical fluctuation and deviations in event rates from adjusting the acceptance window by ± 0.5 mm. A more rigorous study of systematic

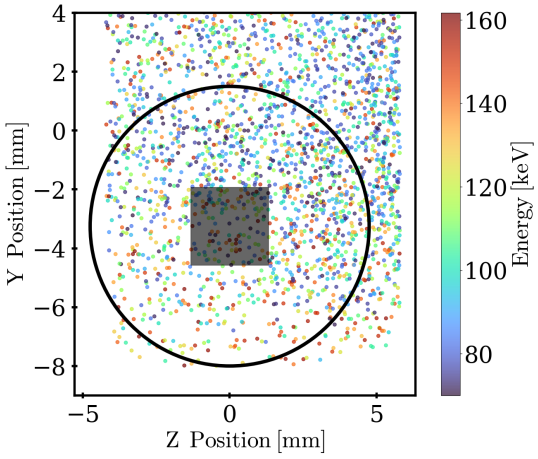

Figure 24: Final location and energy of emitted electrons using 2D particle monitor output in CST. This feature allows for 1 million electrons to be simulated under each setting. The Y position corresponds to the relative height with respect to the electron emission location. The −3.25 mm offset of the diode (overlaid in black) was chosen as its resulting spectrum most closely resembles data, and the relative height is mildly ambiguous in the physical setup. For visibility, only electrons with energy above 70 keV are shown.

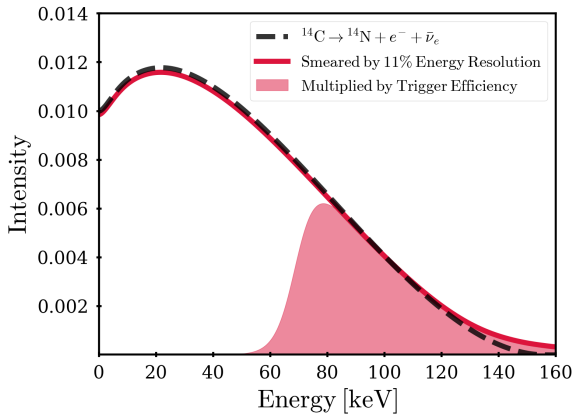

Figure 25: Product of PIN diode trigger efficiency curve and ^{14}C β spectrum (smeared by 11% energy resolution of detector). This curve is discretized and used as a weighting to scale the uniformly-emitted simulation results such that they can be compared directly to data.

uncertainties would be required to fit according to likelihood or another uncertainty-based metric. The horizontal offset of 0.11 kV is an indication that the ^{14}C source disk is not perfectly centered with respect to the drift electrodes, which also explains the lower event rates in data compared to simulation for small symmetric settings in Figure 27. The scaling factor of 1.34 on the detected event rate serves as a general approximation to demonstrate the validity of the simulated model. The $\approx$ 25% discrepancy in event rate is likely due to a confluence of reasons including system alignment, impedance from Teflon structures, smaller-than-expected diode active region, etc. In the following section, we proceed with time of flight estimation.

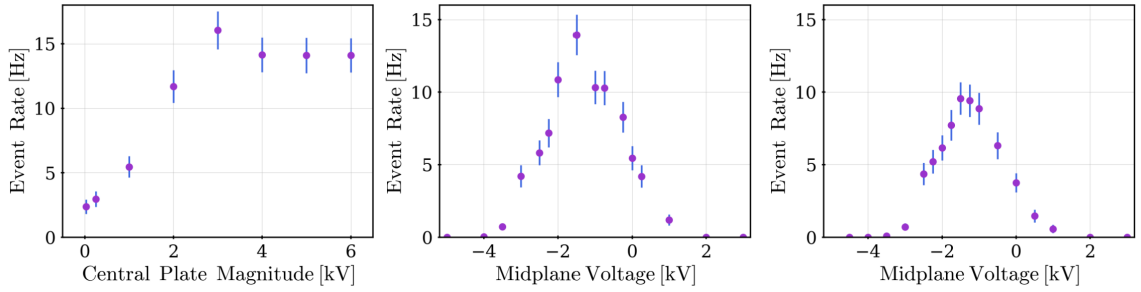

Figure 26: CST simulated event rates scaled according to Figure 25 for (a) symmetric, (b) 2 kV window, and (c) 1 kV window settings. Uncertainty is assigned according to Poisson statistics. Event rates obtained for each setting are higher than in data.

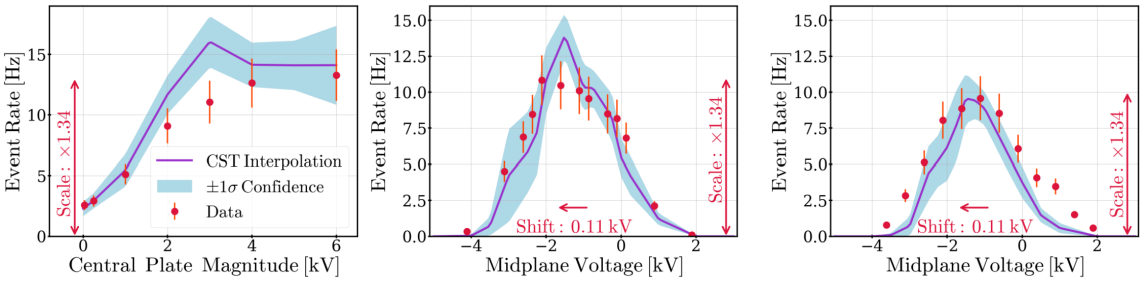

Figure 27: Combined least-squares regression fit of data (red) to interpolated CST rates (purple) for (a) symmetric, (b) 2 kV window, and (c) 1 kV window settings. Scaling factor to data is 1.34 and leftward horizontal offset (applied to 1 kV and 2 kV window results) is 0.11 kV. A ±1 σ confidence interval for simulated event rates accounts for Poisson statistical fluctuations and adjusting the diode active region location by ±0.5 mm. A more detailed systematics study would need to be undertaken in order to fit according to an uncertainty-based metric such as likelihood. Nonetheless, a correspondence between the simulated and detected event rates by a small scaling factor demonstrates the validity of the simulated model.

5.3 Time of Flight Estimation

To evaluate the time of flight of particles in the slow drift region of the demonstrator, we export trajectory information from CST under the largest (± 6 kV) and smallest (±31.25 V) central drift settings studied. The guiding center at each point is tabulated by averaging the electron location over one cyclotron period before/after the point of interest.[3] Time of flight in the slow drift region is then determined based on how long the guiding center is situated between the 25.4 mm central plates. Figure 28 shows that a 70 keV electron can be slowed to less than 1/5 of the maximal drift velocity, being trapped for over 60 ns in the center plate. The drift speed observed in the trajectory is consistent with E/B as evaluated from the simulated fields at each point. Deviations in time of flight occur due to the amount of time a given trajectory spends near the bouncing plates (those that bounce more and reflect nearer to the bouncing plate experience a weaker central drift field

[3] In the relativistic regime, the period in which a particle completes one full orbit due to cyclotron motion is given as $T = \frac{2\pi\gamma m}{qB}$, where m is mass, γ is the Lorentz factor, q is charge, and B is magnetic field strength.

on average than those that bounce fewer times and farther away, therefore having a slightly longer drift time). Simulations with various particle energies confirm the slow drift time of flight largely falls within the range of 54-66 ns, only decreasing slightly in the case of ≥ 130 keV electrons (at which point the cyclotron radius is so large that the electron spends a considerable amount of time under the influence of the outer plate potentials even when its guiding center is situated near the middle). Additional slow drift trajectories are shown in Figure 29. As the electric field produced in the center region is heavily impacted by potentials set on the outer plates for this setup, increasing the dimensions of the slow drift region, thereby reducing fringe field effects, would allow for a slow drift time of flight on the order of μs and largely reduce variations in a given trajectory's time of flight.

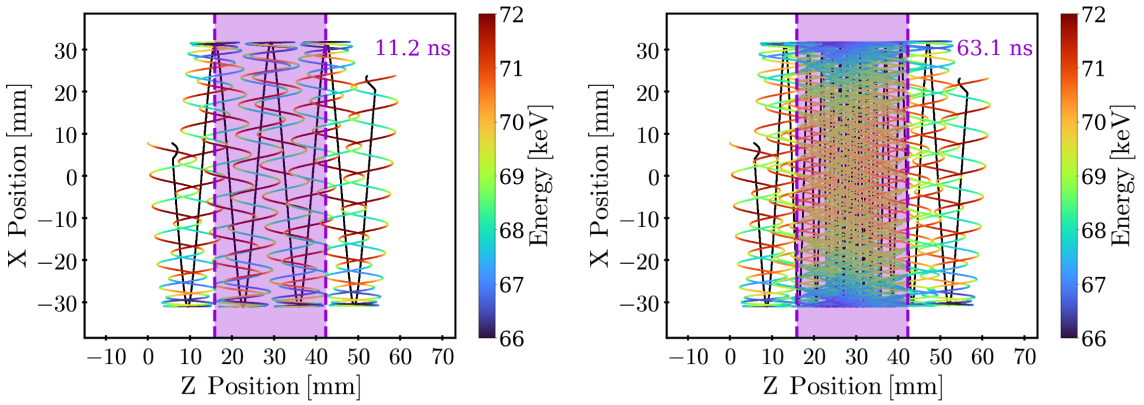

Figure 28: Simulation of 70 keV electron transported with center plates set to (a) ±6 kV and (b) ±31.25 V. Guiding center of trajectory is plotted in black, and the slow drift region is shaded in purple. The amount of time the guiding center is situated in the slow drift region is printed in the top-right corner. The slow drift setting allows one to trap an electron roughly 5-6 times longer than the maximally fast drift setting (63.1 ns in comparison to 11.2 ns).

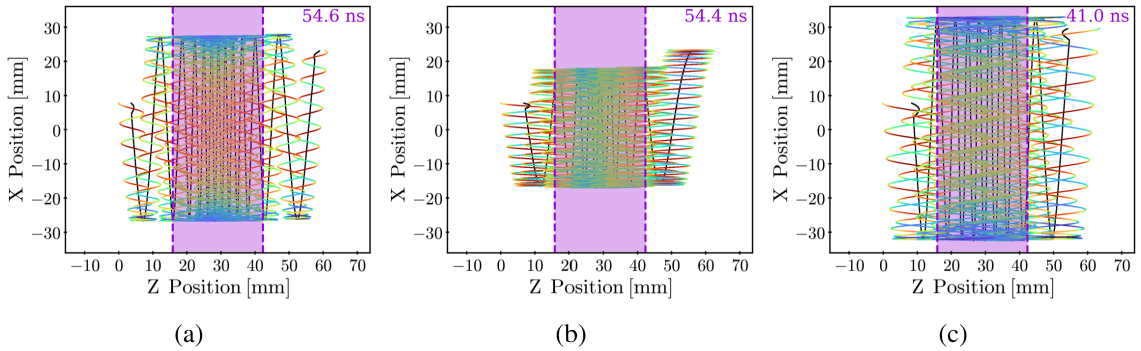

Figure 29: Guiding center and trajectory under ±31.25 V center plate conditions for simulated electrons with energy (a) 30 keV, (b) 100 keV, and (c) 150 keV. The respective times of flight in the center plate region are 54.6 ns, 54.4 ns, and 41.0 ns. In general, time of flight is roughly 54-66 ns for the majority of the spectra, though decreases slightly for exceedingly energetic (≥ 130 keV) electrons.

6 Outlook

The control of β-decay $\mathbf{E}\times\mathbf{B}$ electron drift has been exhibited. Under current operating conditions, we can manipulate drift speed by a factor of 5 (containing electrons for over 60 ns), though would theoretically be able to increase this by orders of magnitude by altering the dimensions of the field cage design. Serving as a demonstration for the RF region of the PTOLEMY detector, future studies will look to incorporate electron injection from a low magnetic field region and instrument an antenna array to perform CRES measurements akin to the studies performed by the Project 8 Collaboration [33] and under development for PTOLEMY [28, 34].

Acknowledgments

This material is based upon work supported by the National Science Foundation Graduate Research Fellowship Program under Grant No.DGE-2039656. Any opinions, findings, and conclusions or recommendations expressed in this material are those of the author(s) and do not necessarily reflect the views of the National Science Foundation. A. Colijn and J. Mead are supported by the Dutch Research Council (NWA.1292.19.231). I. Rago is supported by the MIUR program (CUP:B81I18001170001). C. Tully is supported by the John Templeton Foundation (№ 62313). The authors acknowledge the support of the INFN CSN-V.

References

[1] Y. Fukuda, *et al. Evidence for oscillation of atmospheric neutrinos*, *Physical Review Letters* **81** (1998) 1562–1567.

[2] Q.R. Ahmad, *et al., Direct evidence for neutrino flavor transformation from neutral-current interactions in the Sudbury neutrino observatory*, *Physical Review Letters* **89** (2002) .

[3] KATRIN collaboration, *Direct neutrino-mass measurement based on 259 days of KATRIN data*, 2406.13516.

[4] A. Saenz, S. Jonsell and P. Froelich, *Improved molecular final-state distribution of* het^+ *for the* β*-decay process of* T_2, *Phys. Rev. Lett.* **84** (2000) 242.

[5] L.I. Bodine, D.S. Parno and R.G.H. Robertson, *Assessment of molecular effects on neutrino mass measurements from tritium* β *decay*, *Phys. Rev. C* **91** (2015) 035505.

[6] F. Fränkle, A. Schaller, K. Blaum, L. Bornschein, G. Drexlin, F. Glück et al., *Katrin background due to surface radioimpurities*, *Astroparticle Physics* **138** (2022) 102686.

[7] PTOLEMY collaboration, *PTOLEMY: a proposal for thermal relic detection of massive neutrinos and directional detection of MeV dark matter*, 1808.01892.

[8] Project 8 collaboration, *The Project 8 neutrino mass experiment*, 2203.07349.

[9] A.G. Cocco, G. Mangano and M. Messina, *Probing low energy neutrino backgrounds with neutrino capture on beta decaying nuclei*, *Journal of Physics: Conference Series* **110** (2008) 082014.

[10] PTOLEMY collaboration, *Neutrino physics with the PTOLEMY project: active neutrino properties and the light sterile case*, *Journal of Cosmology and Astroparticle Physics* **2019** (2019) 047.

[11] Y. Cheipesh, V. Cheianov and A. Boyarsky, *Navigating the pitfalls of relic neutrino detection*, *Phys. Rev. D* **104** (2021) 116004.

[12] S. Nussinov and Z. Nussinov, *Quantum induced broadening: A challenge for cosmic neutrino background discovery*, *Phys. Rev. D* **105** (2022) 043502.

[13] Z. Tan and V. Cheianov, *Importance of the X-ray edge singularity for the detection of relic neutrinos in the PTOLEMY project*, *SciPost Phys.* **17** (2024) 022.

[14] PTOLEMY collaboration, *Heisenberg's uncertainty principle in the ptolemy project: A theory update*, *Phys. Rev. D* **106** (2022) 053002.

[15] B. Monreal and J.A. Formaggio, *Relativistic cyclotron radiation detection of tritium decay electrons as a new technique for measuring the neutrino mass*, *Phys. Rev. D* **80** (2009) 051301.

[16] Project 8 collaboration, *Single-electron detection and spectroscopy via relativistic cyclotron radiation*, *Phys. Rev. Lett.* **114** (2015) 162501.

[17] Project 8 collaboration, *Tritium beta spectrum measurement and neutrino mass limit from cyclotron radiation emission spectroscopy*, *Phys. Rev. Lett.* **131** (2023) 102502.

[18] PTOLEMY collaboration, *A design for an electromagnetic filter for precision energy measurements at the tritium endpoint*, *Progress in Particle and Nuclear Physics* **106** (2019) 120.

[19] PTOLEMY collaboration, *Implementation and optimization of the PTOLEMY transverse drift electromagnetic filter*, *Journal of Instrumentation* **17** (2022) P05021.

[20] M. Rajteri, M. Biasotti, M. Faverzani, E. Ferri, R. Filippo, F. Gatti et al., *TES Microcalorimeters for PTOLEMY*, *J. Low Temp. Phys.* **199** (2019) 138.

[21] S. Weinberg, *Universal neutrino degeneracy*, *Phys. Rev.* **128** (1962) 1457.

[22] L. Osorio-Quiroga, G. Grime, M. Roberto, R. Viana, Y. Elskens and I. Caldas, $\boldsymbol{E} \times \boldsymbol{B}$ *drift particle transport in tokamaks*, *Brazilian Journal of Physics* **53** (2023) .

[23] J. Ekholm and W. Hargus, $\boldsymbol{E} \times \boldsymbol{B}$ *Measurements of a* 200 *xenon Hall thruster*, *41st AIAA/ASME/SAE/ASEE Joint Propulsion Conference & Exhibit* (2012) .

[24] K. Stasiewicz and B. Eliasson, *Ion acceleration to* 100 *keV by the* $\boldsymbol{E} \times \boldsymbol{B}$ *wave mechanism in collision-less shocks*, *Monthly Notices of the Royal Astronomical Society* **508** (2021) 1888.

[25] M. Singer, M.R. Stoneking, E.V. Stenson, S. Nißl, A. Deller, A. Card et al., *Injection of positrons into a dense electron cloud in a magnetic dipole trap*, *Physics of Plasmas* **28** (2021) 062506.

[26] N. Savard, A. Groutso, S. Melanson, D. Potkins and M. Dehnel, *Trapping secondary electrons in* $\boldsymbol{E} \times \boldsymbol{B}$ *drift for an alpha generating penning ion source*, *Journal of Physics: Conference Series* **2244** (2022) 012104.

[27] K. Valerius, H. Hein, H. Baumeister, M. Beck, K. Bokeloh, J. Bonn et al., *Prototype of an angular-selective photoelectron calibration source for the KATRIN experiment*, *Journal of Instrumentation* **6** (2011) P01002.

[28] Y. Iwasaki, A. Tan and C.G. Tully, *Towards CRES-based non-destructive electron momentum estimation for the PTOLEMY relic neutrino detector*, 2404.00817.

[29] C. Strobel, G. Gantefoer, A. Bodi and P. Hemberger, *A magnetic bottle time-of-flight electron spectrometer suitable for continuous ionization sources*, *Review of Scientific Instruments* **90** (2019) 063105.

[30] Dassault Systèmes, "CST Studio Suite 2024." https://www.3ds.com/products/simulia/cst-studio-suite.

[31] R.H.V. Malat, *Effect of vacuum conditions on breakdown voltage between electrodes in vacuum.*, *Czechoslovak Journal of Physics* **30** (1980) 518.

[32] S. Wüstling, T. Armbrust, M. Steidl and S. Zadorozhny, *A large, 64-pixel PIN-diode detector for low-energy beta-electrons*, *Nuclear Instruments and Methods in Physics Research Section A: Accelerators, Spectrometers, Detectors and Associated Equipment* **568** (2006) 382.

[33] A. Ashtari Esfahani, S. Böser, N. Buzinsky, M. Carmona-Benitez, C. Claessens, L. de Viveiros et al., *Real-time signal detection for cyclotron radiation emission spectroscopy measurements using antenna arrays*, *Journal of Instrumentation* **19** (2024) P05073.

[34] L. Pesce, *Cyclotron radiation detection in the electron trap for the PTOLEMY experiment*, Master's thesis, Sapienza University of Rome, 2024.

Supplementary Material

A Beta Spectrometer

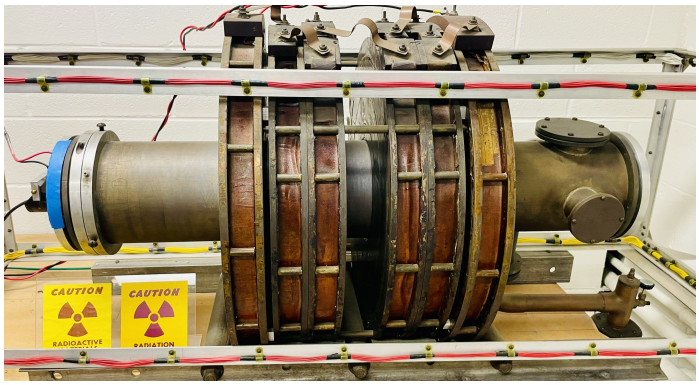

Figure 30: Photograph of the full spectrometer setup used in the experiment. The system includes a vacuum chamber, magnetic lenses, and shielding components arranged to guide and focus electron trajectories for precise beta spectroscopy.

The beta spectrometer used in this study is a magnetic lens spectrometer, designed to analyze beta decay energy spectra by selectively filtering electrons based on their momenta (Figure 30). It consists of a vacuum chamber, a magnetic lens system, and the PIN diode as the detector. The vacuum chamber ensures minimal scattering of beta particles at about 1 mTorr. The spectrometer's magnetic lens system, configured in a long solenoidal arrangement, generates a cylindrically symmetric magnetic field, guiding beta particles along helical trajectories. By adjusting the field strength, electrons of specific momenta are focused onto the detector, as illustrated in the simulated trajectories in Figure 31. This configuration sets a constant momentum resolution of 2.45% (σ/μ).

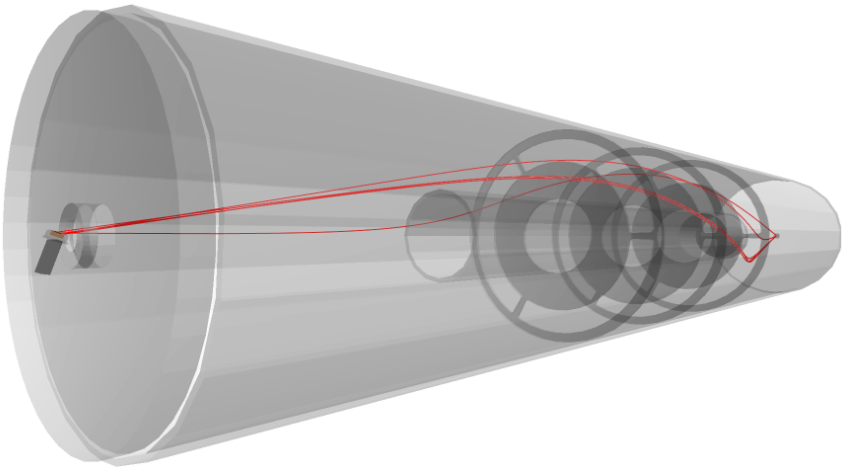

Figure 31: Simulated electron trajectories within the spectrometer. The red lines represent 70 keV electrons traversing the magnetic lenses, influenced by applied magnetic fields with 3 A coil currents.

The PIN diode was positioned at the spectrometer's exit plane to record beta particles after magnetic field selection, as shown in Figure 32 (left). The system is calibrated using a ^{137}Cs

source, which provides a well-defined reference energy for momentum calibration. A Kapton thin-film window at the spectrometer's entry minimizes electron energy loss while maintaining vacuum integrity, ensuring accurate energy calibration. Additionally, external magnetic trim coils compensate for stray fields, ensuring a stable and reproducible spectrometric response.

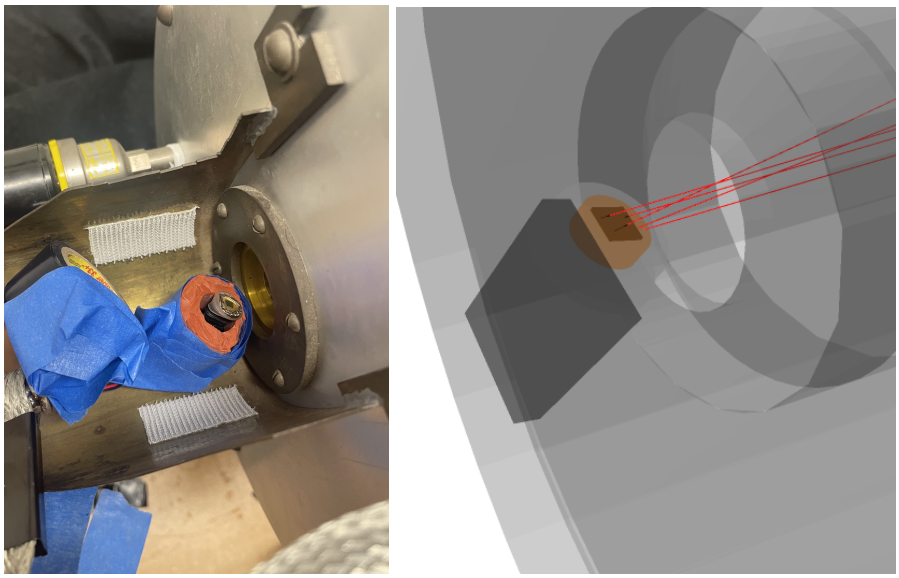

Figure 32: (Left) Calibration setup showing the PIN diode and magnetic lens system during alignment and testing. (Right) Simulated electron trajectories under calibration conditions, focusing on the PIN diode region where electron paths converge and interact with the detector's surface for precise momentum calibration.